Nanoscale

ROYAL SOCIETY OF CHEMISTRY

PAPER

View Article Online
View Journal | View Issue

Check for updates

Cite this: *Nanoscale*, 2025, **17**, 25071

Europium intercalation as a route to modulate electronic and magnetic properties of *h*-BN/Ni(111)

Elena Voloshina, *[a] Frederik Schiller, *[b] Khadiza Ali, [c,d] Alaa Mohammed Idris Bakhit, [b,e,f] Rodrigo Castrillo-Bodero,[b] Beate Paulus[g] and Yuriy Dedkov *[h]

Received 13th September 2025,
Accepted 17th October 2025

DOI: 10.1039/d5nr03875h

rsc.li/nanoscale

We present a combined density functional theory (DFT) and photoelectron spectroscopy (PES) study of the electronic and magnetic properties of the intercalation-like system, where europium (Eu) is intercalated at the interface between hexagonal boron nitride (*h*-BN) and a Ni(111) substrate. From the theory side two interface models are considered: (i) a sharp *h*-BN/Eu/Ni(111) structure and (ii) an interfacial $EuNi_5$ alloy. In both cases, Eu intercalation restores the π-band dispersion of *h*-BN and induces doping effects, with the energy shift of the π-band at the Γ point found to be highly sensitive to the interfacial structure. Our results show that Eu retains a localized magnetic moment in both configurations, with distinct coupling to the substrate. Simulated B 1s and N 1s core-level shifts and near-edge X-ray absorption spectra provide further insights into the local bonding environment and interfacial interaction strength. Further systematic electron diffraction and PES experiments support the formation of the sharp *h*-BN/Eu/Ni(111) interface as derived from the matching of experimentally derived positions of B 1s and N 1s core-levels as well as valence bands dispersions to the theoretical results. These findings offer a framework for understanding the role of rare-earth intercalation in tuning the properties of 2D/metal interfaces and pave the way for future spintronic applications.

1 Introduction

Two-dimensional (2D) materials interfaced with metals and semiconductors form a unique class of heterostructures that enable the control and manipulation of electronic and magnetic properties at the atomic scale.[1–5] Among such materials, hexagonal boron nitride (*h*-BN) stands out due to its wide band gap (~5.7–6 eV (ref. 6 and 7)), mechanical robustness, and chemical inertness. Its structural similarity to graphene and its ability to form atomically sharp interfaces with a range of metals and semiconductors make *h*-BN an ideal spacer and protective layer in van der Waals (vdW) heterostructures.[3,5,8,9] This functionality is especially relevant in the context of spintronics, where minimizing spin scattering at interfaces is essential for achieving long spin lifetimes and efficient spin injection.

When deposited on transition metal substrates, such as Ni(111), *h*-BN exhibits strong hybridization with the metal d states, leading to significant modifications in its electronic structure. For instance, a pronounced hybridization between Ni 3d and *h*-BN π states at the *h*-BN/Ni(111) interface was demonstrated,[10–12] resulting in a breakdown of the insulating nature of *h*-BN and the formation of interface states near the Fermi level.[10] This interaction not only alters the band structure of *h*-BN, but also has implications for its use as a tunnel barrier or spin-filtering layer in spintronic devices.

To overcome such strong hybridization and to tailor interfacial properties in a controlled fashion, intercalation of atoms between *h*-BN and the underlying metal has emerged as a promising strategy. While intercalation of noble metals (Au, Ag, Cu) has been widely studied for electronic decoupling, more reactive species such as alkali, alkaline-earth, and rare-earth elements offer a broader functional palette by introducing charge transfer, mag-

---

[a] *Division of Theoretical Physics, Ruđer Bošković Institute, Bijenička cesta 54, 10000 Zagreb, Croatia. E-mail: elena.voloshina@irb.hr*
[b] *Centro de Física de Materiales (CSIC-UPV/EHU) and Material Physics Center (MPC), 20018 Donostia-San Sebastián, Spain. E-mail: frederik.schiller@csic.es*
[c] *Chalmers University of Technology, Göteborg, Chalmersplatsen 4, 412 96 Göteborg, Sweden*
[d] *Department of Physics, BITS Pilani, Hyderabad Campus, Hyderabad, 500078 Telangana, India*
[e] *Departamento de Física de Materiales, Universidad del País Vasco (UPV/EHU), 20018 Donostia-San Sebastián, Spain*
[f] *Donostia International Physics Center (DIPC), 20018 Donostia-San Sebastián, Spain*
[g] *Institut für Chemie und Biochemie, Freie Universität Berlin, Arnimallee 22, 14195 Berlin, Germany*
[h] *Center for Advanced Laser Techniques, Institute of Physics, Bijenička cesta 46, 10000 Zagreb, Croatia. E-mail: ydedkov@ifs.hr*

netism, or alloy formation at the interface.[3] Among these, europium (Eu) is particularly attractive due to its ability to adopt multiple valence states and exhibit strong localized magnetic moments in the divalent Eu^{2+} state.[13]

Recent experimental work by Bakhit *et al.* investigated the intercalation of Eu beneath a monolayer of *h*-BN grown on a Pt(111) substrate.[13] Upon intercalation, a well-defined 2D $EuPt_2$ surface alloy was formed at the interface, exhibiting divalent Eu ions and clear signatures of ferromagnetic ordering at low temperatures. Remarkably, the magnetic behavior was preserved even after partial exposure to ambient conditions, underscoring the protective role of the *h*-BN overlayer. This study demonstrated that the intercalation process not only decouples *h*-BN from the substrate but also induces emergent magnetic properties at the buried interface – properties that are tunable *via* structural control of the intercalated layer.

Building on this concept, our present work presents a combined first-principles theoretical and spectroscopic investigation of Eu intercalation at the *h*-BN/Ni(111) interface. While Eu intercalation beneath *h*-BN has been previously studied in the context of noble metal substrates, its behavior on ferromagnetic Ni(111), with its strong 3d magnetism and known hybridization with *h*-BN valence band states, remains largely unexplored. Moreover, the possibility of Eu forming an interfacial alloy with Ni – in particular, $EuNi_5$ – type configurations – adds a new dimension to the interplay between electronic structure, magnetic ordering, and interfacial bonding.

In our theoretical analysis we consider two distinct models for the Eu intercalation system: a sharp *h*-BN/Eu/Ni(111) interface, and a more complex structure involving the formation of a $EuNi_5$ alloy at the interface. Using density functional theory (DFT), we analyze how each configuration modifies the electronic band structure of the *h*-BN layer, particularly focusing on the restoration or shift of its π bands at the Γ point. Our results reveal that Eu intercalation, in both configurations, leads to partial electronic decoupling of the *h*-BN overlayer – restoring the π-characteristic bands that are otherwise suppressed by direct contact with Ni (111). These calculations are complemented by the simulation of the core-level shifts (CLS) for the B 1s and N 1s states, as well as near-edge X-ray absorption fine structure (NEXAFS) spectra for both nitrogen and boron K-edges. The following experiments indicate the formation of the sharp *h*-BN/Eu/Ni(111) interface as revealed from low-energy electron diffraction (LEED) and photoelectron spectroscopy (PES) results. Our findings provide theoretical and spectroscopic benchmarks for interpreting future results on the studies of rare-earth intercalated 2D systems, with implications for spintronics, tunnel junctions, and quantum materials design.

2 Theoretical and experimental details

2.1 Theory

Spin-polarised DFT calculations based on plane-wave basis sets of 500 eV cut-off energy were performed with the Vienna *ab initio* simulation package (VASP).[14,15] The Perdew–Burke–Ernzerhof (PBE) exchange–correlation functional[16] was employed. The electron-ion interaction was described within the projector augmented wave (PAW) method[17] with B (2s, 2p), N (2s, 2p), Ni (3d, 4s), and Eu (5s, 5p, 4f, 6s) states treated as valence states. The Brillouin-zone integration was performed on Γ-centred symmetry reduced Monkhorst–Pack mesh using a Methfessel–Paxton smearing method of first order with σ = 0.15 eV, except for the calculations of total energies. For those calculations, the tetrahedron method with Blöchl corrections[18] was used. When studying bulk *h*BN, a 24 × 24 × 6 *k*-mesh was used. For the freestanding *h*BN monolayer and *h*BN/Ni(111) interface, 24 × 24 × 1 *k*-meshes were used. In the case of larger supercells the number of *k*-points was reduced accordingly. Dispersion interactions were included by means of the DFT-D2 correction method.[19] The DFT+*U* scheme[20] was adopted for the treatment of Eu 4f orbitals, with the Coulomb parameters of U = 7 eV and J = 1 eV that are known to be well suited to describe rare earth systems.[21,22] Selected calculations were performed using the Heyd, Scuseria, and Ernzerhof (HSE) hybrid functional.[23] The convergence criteria for energy was set equal to 10^{-5} eV.

The studied interfaces were modelled by symmetric slabs with a vacuum gap of at least 19.5 Å. The lattice constant in the lateral plane was set according to the optimised value of bulk Ni ($a_{\mathrm{Ni}(111)}$ = 2.488 Å). This way the mismatch between the *h*-BN and substrate lattices is less than 1%. The used supercells contain 13 layers of Ni and 1 ML-BN adsorbed on both sides of the slab. In the case of BN–Eu–Ni(111) systems, Eu atoms are added between the *h*-BN monolayer and Ni(111). For all these structures the atoms of the 9 middle inner layers were fixed at their bulk positions during the structural optimisation procedure, whereas the positions of all other atoms were fully relaxed until forces became smaller than 0.01 eV $Å^{-1}$. For the calculations using hybrid functional, an asymmetric BN/Ni(111) slab is used and the number of Ni(111) layers is reduced till 7.[12]

The adsorption energy between BN and substrate is defined as the difference between the total energy of the BN/substrate system, $E_{\mathrm{BN/sub}}$, and that of the adsorbate and substrate in isolation, E_{BN} and E_{sub}, respectively: $E_{\mathrm{ads}} = (E_{\mathrm{BN/sub}} - 2 \times E_{\mathrm{BN}} - E_{\mathrm{sub}})/2A$.[24] Here: A is the number of BN units and the factor 2 accounts for the presence of two identical interfaces in the structural model.

The core level binding energies were calculated within the initial-state approximation, where the valence electrons are kept frozen during photoionisation.

The NEXAFS spectra simulations were obtained within the Mahan–Nozierś–De Dominicis (MND) theory of dynamical core-hole screening using the ELSA-software[25] according to the procedure described in ref. 26 and 27. To obtain an input for the NEXAFS spectra simulations, we employed large supercells of (6 × 6) and $(4\sqrt{3} \times 4\sqrt{3})R30°$ periodicity when studying free-standing monolayer of *h*-BN, BN/Ni(111), BN/Eu/Ni(111) and $BN/EuNi_5/Ni(111)$ systems, respectively.

2.2 Experiment

Samples preparation and PES experiments were performed at the VUV-Photoemission beamline of Elettra Synchrotron in Trieste, Italy. The Ni(111) single crystal, used as a substrate, was cleaned by sputtering/annealing cycles ($p(\text{Ar}^+) = 2 \times 10^{-5}$ mbar, 1.0 keV, 15 min/800 °C, 15 min) until a sharp hexagonal LEED pattern was observed. Followed the cleaning routing, the *h*-BN layer was formed by exposing the Ni(111) substrate kept at 800 °C to borazine precursor ($B_3H_6N_3$, KATCHEM spol. s r. o.) at a pressure of 5×10^{-6} mbar for 15 min. The intercalation of Eu metal was achieved *via* its deposition from the carefully degased and calibrated metal evaporator on *h*-BN/Ni(111), hold at room temperature, followed by the sample annealing at 300 °C for 25 min. At every preparation step the ordering and cleanness of the formed system was verified using LEED and XPS, respectively.

In XPS and ARPES experiments the Scienta R4000 analyser combined with 2D-CCD detector was used. The total energy resolution in XPS measurements was set to 150 meV (beamline and spectrometer). In ARPES experiments the energy resolution was set to 40 meV (analyser) and angular resolution was 0.1°.

3 Results and discussion

Bulk hexagonal boron nitride, *h*-BN, crystallises in the hexagonal $P6_3/mmc$ space group. It is an sp^2-bonded layered material in which individual layers are held together by van der Waals forces. The experimental lattice parameters of *h*-BN (a^{expt} = 2.504 Å and c^{expt} = 6.656 Å)[28] are well reproduced by DFT (here: PBE+D2): a^{DFT} = 2.506 Å and c^{DFT} = 6.825 Å. This allows to consider the parent *h*-BN/Ni(111) system without lattice mismatch at the interface (see Fig. 1(a)).

Yet, a correct description of the band structure of *h*-BN presents a great challenge for theoretical methods. *h*-BN is a wide band gap semiconductor with experimentally measured low-temperature indirect band gap of E_g = 5.955 eV.[29] A decrease in dimensionality leads to an increase in E_g[30] and for a monolayer *h*-BN it is direct and located at the *K* point. GGA functionals severely underestimate the band gap. Fig. 2(a) shows the band structure of a monolayer *h*-BN obtained with PBE functional and the E_g in this case is equal to 4.67 eV. The DFT+*U* approach, which successfully overcomes the band gap problem when studying rare-earth and transition metal compounds, is useless in the case of *h*-BN with its sp valence band states.

One possible solution is to use hybrid functionals.[31] Fig. 2(b) shows the band structure of a monolayer *h*-BN obtained with HSE functional and the E_g in this case is equal to 6.08 eV. However, while powerful for describing a *h*-BN band structure, hybrid functionals present a significant computational challenge when applied to metallic systems.[32] This problem can be attributed to the oversimplified Hartree Fock-like exchange energy included in the hybrid functionals, which is known to give an inaccurate description of the electronic structure near the Fermi level.[33] The introduction of a short-range Coulomb potential, as in the case of the HSE functional, does indeed alleviate some of the problems,[23,33,34] but the fundamental difficulties remain the same. In our earlier work we performed band structure calculations with the HSE functional for multilayer *h*-BN on Ni(111).[12] The obtained results allowed us to conclude that while the HSE functional is much better than the PBE functional in predicting the band gaps, for both computational schemes (HSE and PBE) the qualitative results are similar (*cf.* Fig. 2(c) and (d)). At the same time, utilisation of the HSE functional leads to inaccuracies in the

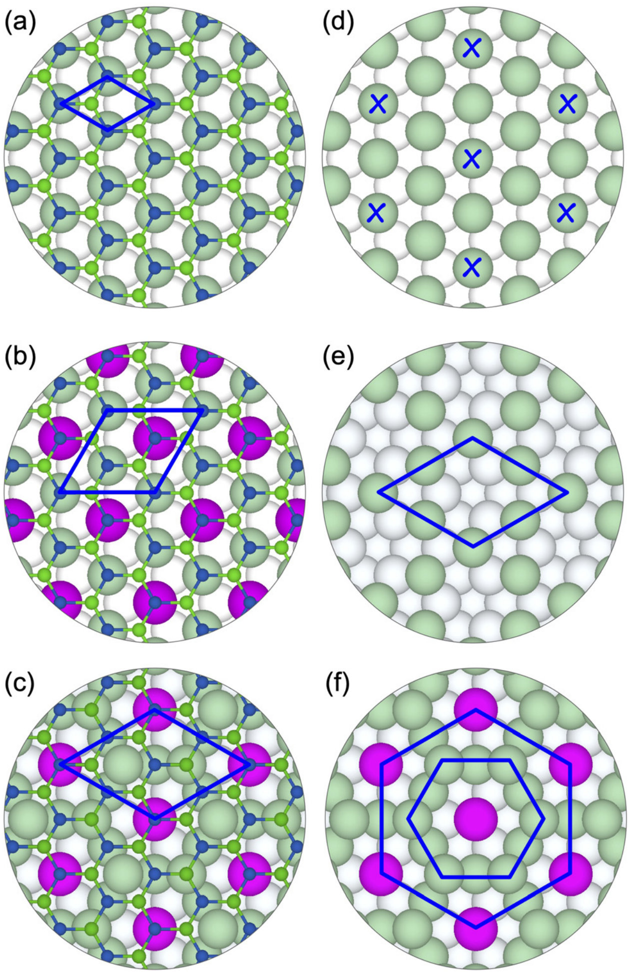

Fig. 1 Top views of the crystallographic structures of the studied systems: (a) *h*-BN/Ni(111); (b) *h*-BN/Eu/Ni(111); (c) *h*-BN/EuNi$_5$/Ni(111). Blue rhombus indicate the corresponding unit cells. Spheres of different size and colour represent atoms of different types: small blue and green spheres represent N and B, respectively; large green spheres highlight Ni atoms of the interface layer, the remaining Ni atoms are shown with light grey spheres; large pink spheres are intercalated Eu atoms. (d–f) Evolution of the interface Ni-layer during formation of a thin-layer EuNi$_5$ alloy: every second Ni atom from the interface layer in every second row, marked in (d) with crosses, is removed; this results in a (2 × 2) overstructure (indicated with blue rhombus in (e)). Eu atoms are placed above the created vacancies (f) and residual Ni-atoms form hexagons around the Eu sites as shown with small hexagon. The resulting overstructure is highlighted with large hexagon.

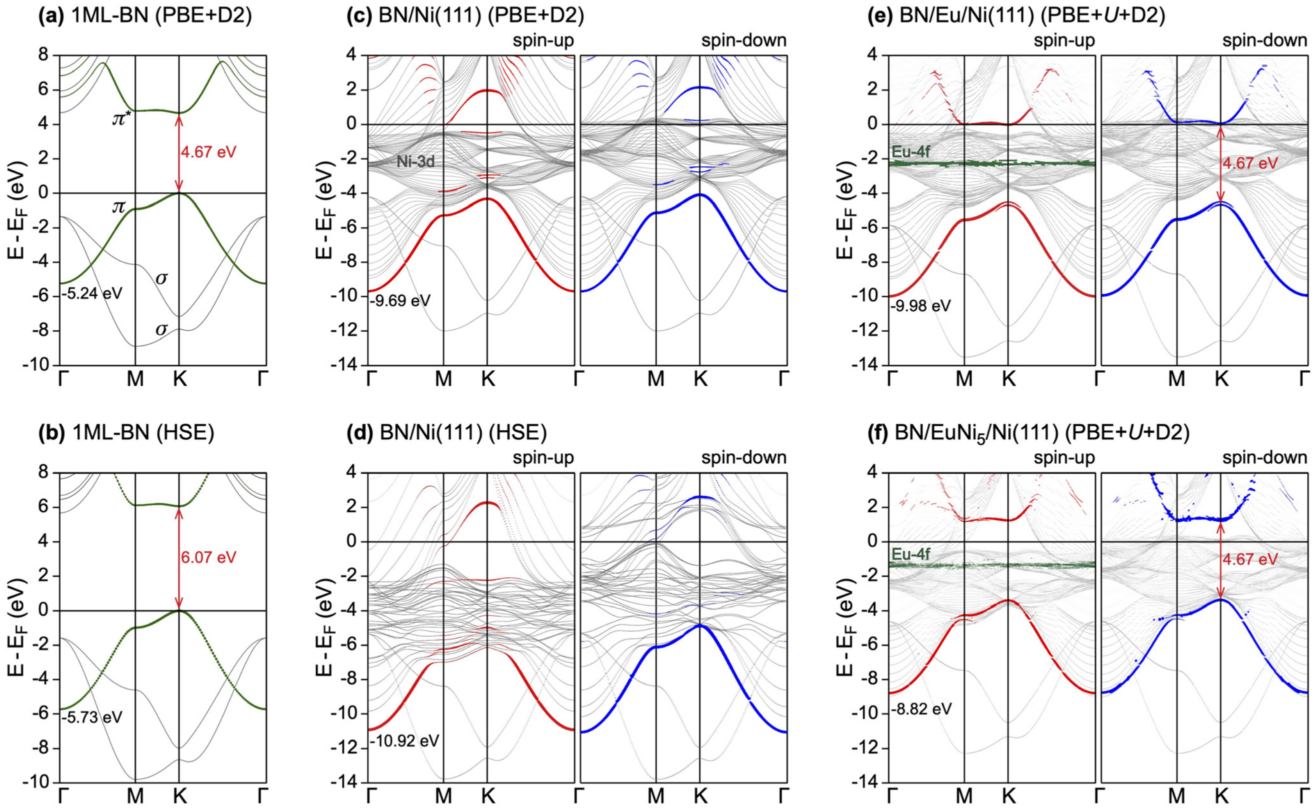

Fig. 2 Band structures of (a and b) a free-standing *h*-BN monolayer calculated using the PBE+D2 and HSE approaches; (c and d) BN/Ni(111) calculated using the PBE+D2 and HSE approaches; (e) BN/Eu/Ni(111) calculated using the PBE+*U*+D2 approach; (f) BN/EuNi$_5$/Ni(111) calculated using the PBE+*U*+D2 approach. The weight of the BN-π character is highlighted by the size of filled circles superimposed with the plot of the band structure. The energy gap between π and π* states is indicated in (a)–(f). The energy position of the π state at *Γ* point is indicated at each subplot.

description of fundamental properties of metal, which are determined by electronic structure near the Fermi energy (enlarged valence bandwidth, greatly suppressed density of states at the Fermi level, enhanced magnetic moments, *etc.*). These observations together with increased computational cost when studying large supercells make the hybrid-functional approach potentially impractical for the present study. Therefore, we decided to stick with the PBE(+*U*+D2) approach in our studies, always keeping in mind the possible inaccuracies in the prediction of the energy gap between the π and π* bands of *h*-BN and focusing specifically on the relative changes in the electronic structure of the systems under study rather than on the absolute energies of the valence band states.

We first discuss the structural and electronic properties of a *h*-BN monolayer grown on Ni(111) as a reference system (see its crystallographic structure in the SI). A single *h*-BN layer is adsorbed on Ni(111) in the top-fcc arrangement, where the N-atom of *h*-BN is placed above the Ni-atom of the interface layer, while the B-atom occupies the fcc hollow adsorption site of Ni(111) (Fig. 1(a)).[11,12,35] The calculated mean distance between *h*-BN and Ni(111) is 2.043 Å (Fig. 3(a)). At that, N- and

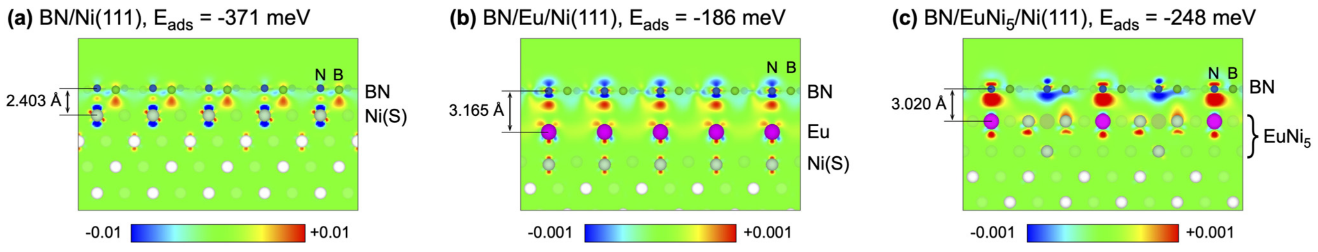

Fig. 3 Side views of different Eu-based intercalation structures: (a) parent BN/Ni(111), (b) BN/Eu/Ni(111), (c) BN/EuNi$_5$/Ni(111). This side views are taken along the BN arm-chair edge and they are overlaid with electron charge difference maps $\Delta\rho(r) = \rho_{BN/sub}(r) - \rho_{BN}(r) - \rho_{sub}(r)$ (sub: substrate). $\Delta\rho$ is colour coded as blue (-0.01 e Å^{-3}), green (0), and red (0.01 e Å^{-3}) and (-0.001 e Å^{-3}), green (0), and red (0.001 e/Å^{-3}), for (a) and (b and c), respectively. The corresponding adsorption energy (E_{ads}, in meV per BN-unit cell) as well as the mean equilibrium distance between BN and substrate are given at each subplot.

B-atoms are separated from the Ni interface differently: $d_{\text{B–Ni(111)}} = 1.983$ Å and $d_{\text{N–Ni(111)}} = 2.103$ Å.

The band structure of *h*-BN/Ni(111) is shown in Fig. 2(c), where it is overlaid with the weight of the BN-π band shown by red/blue lines for spin-up/down channels, respectively. The charge transfer from Ni(111) to a *h*-BN monolayer (Fig. 3(a)) leads to the *n*-doping of *h*-BN with a significant downward shift of the BN-derived π states, followed by the effective overlap of the orbitals of BN and the substrate, especially Ni 3d states with an out-of-plane component (Ni-d_{z^2}, Ni-d_{xz}, Ni-d_{yz}). This in turn leads to the emergence of hybrid interface states with the predominant Ni-3d character. As a consequence of the overlap of the electronic states at the *h*-BN/Ni(111) interface, the magnetic moment on B/N atoms appears: $m_{\text{N}} = 0.017\mu_{\text{B}}$ and $m_{\text{B}} = -0.008\mu_{\text{B}}$, respectively. These data are comparable to the magnetic moments of C in graphene/Ni(111). Following the experimental works on detecting induced magnetism in graphene on Ni(111) using XMCD,[36,37] it is expected that a similar induced magnetic moment in *h*-BN on Ni(111) can also be observed. Along with that the magnetic moment of the Ni(S) atoms at the interface is strongly reduced to $0.55\mu_{\text{B}}$ compared to the value of $0.71\mu_{\text{B}}$ and $0.64\mu_{\text{B}}$ for the clean Ni (111) surface and Ni-bulk, respectively. These values of magnetic moments of Ni (both bulk and surface) are in very good agreement with previously published experimental and calculated data.[36,38–41] All these observations correlate with strong interaction at the interface: $E_{\text{int}} = -372$ meV per BN unit cell.

The intercalation of Eu into the *h*-BN/Ni(111) interface might lead to two possible outcomes: (1) formation of a sharp *h*-BN/Eu/Ni(111) interface, and (2) formation of thin layer of an EuNi$_x$ alloy at the interface between *h*-BN and Ni(111) stack.

In case of a sharp *h*-BN/Eu/Ni(111) interface, similarly to the graphene/Eu/Ni(111) stack,[22] a $(\sqrt{3} \times \sqrt{3})R30°$ symmetry with respect to BN/Ni(111) is assumed. Such superstructure is compatible to the experimental observations described below and in accordance to similar systems like Eu/BN/Pt(111)[13] or Eu/BN/Ir(111).[42] Considering possible crystallographic structures of this intercalation-like system, one can see that the Eu atoms below the *h*-BN monolayer can be placed either in the FCC or in the HCP hollow sites of the Ni(111) slab or above the interfacial (TOP) nickel atoms. Our calculations demonstrate that the TOP arrangement (Fig. 1(b)) is significantly (by *ca.* 250 meV per unit cell) more stable from an energetic point of view than the other two cases under study (see the crystallographic structure in the SI).

Intercalation of Eu between the *h*-BN monolayer and Ni (111) leads to the decoupling of the electronic states of BN from that of the Ni substrate (Fig. 2(e)). BN in the BN/Eu/Ni (111) system is *n*-doped due to the partial transfer of the mobile Eu-6s electrons on the π* states of BN (Fig. 3(b)). The strong charge transfer from Eu atoms on BN is compensated by the respective electron transfer from the underlying Ni layer on Eu atoms, leading to the dramatic decrease of the magnetic moments of the Ni-interface atoms ($0.37\mu_{\text{B}}$) and to the negligible moments of B/N-atoms ($0.006/0.003\mu_{\text{B}}$), compared to the parent *h*-BN/Ni(111) system. This charge redistribution leads also to the shift of the Eu-4f level by ≈90 meV to the smaller binding energies as compared to the uncovered substrate. Another consequence of the above perturbations is the appearance of the almost flat band located in the vicinity of E_{F} along the *K–M* direction of the Brillouin zone. In the rest, since there is no hybridisation between the valence band states of BN and the substrate, the energy dispersion of the *h*-BN-derived π states resembles the one for the free-standing *h*-BN monolayer, although shifted in energy (*cf.* Fig. 2(e) and (a)).

The interaction of BN with the Eu/Ni(111) substrate is significantly weaker than it was before the Eu intercalation: $E_{\text{ads}} = -186$ meV per BN unit cell. This value correlates with the relatively large distance between almost entirely flat *h*-BN monolayer and the substrate of 3.165 Å (Fig. 3(b)).

Let us now consider the formation of an EuNi$_x$ alloy at the *h*-BN/Ni(111) interface. It has been experimentally established that the deposition of Eu onto a clean Ni(111) surface followed by thermal annealing leads to the formation of an ordered surface compound with a stoichiometry close to EuNi$_5$.[43] Thus, we assume that a thin EuNi$_5$ layer might be formed at the interface between BN and Ni(111) upon Eu intercalation.

EuNi$_5$ crystallises in the CaCu$_5$ structure (space group *P*6/*mmm*) and is composed of two different atomic layers, one containing of only Ni and the other of both Ni and Eu atoms. The optimised lattice constants ($a^{\text{DFT}} = 4.974$ Å and $c^{\text{DFT}} = 3.932$ Å, DFT: PBE+D2+*U*) are in a good agreement with experimental values of $a^{\text{expt}} = 4.905$ Å and $c^{\text{expt}} = 3.948$ Å.[44] In the pure Ni layer of EuNi$_5$, Ni atoms are organised in a kagome lattice with the nearest neighbour Ni–Ni distances of approximately the same length as for the Ni(111) surface ($d_{\text{Ni–Ni}}^{\text{EuNi}_5} = 2.487$ Å and $d_{\text{Ni–Ni}}^{\text{Ni(111)}} = 2.488$ Å, *i.e.*, the mismatch between the Ni(111) and EuNi$_5$ lattices is less than 0.05%). In the next layer, which composition corresponds to the formula EuNi$_2$, Eu atoms are located above the centres of the Ni-hexagons, whereas the Ni-atoms occupy the hollow sites above the Ni-triangles. Thus, each Eu-atom is surrounded by a Ni-hexagon of the same size as in the pure Ni-layer. These two hexagons are located exactly on top of each other, but rotated by 30° with respect to each other.

In order to model the formation of a thin layer of EuNi$_5$ alloy at the BN/Ni(111) interface, we remove every second Ni atom from the interface layer in every second row (see Fig. 1(d)). This results in a (2 × 2) overstructure that completely corresponds to the pure Ni-layer of EuNi$_5$ (see Fig. 1(e)). To form the EuNi$_2$ layer of EuNi$_5$, we place Eu atom above the created vacancies in the interface Ni-layer and place residual Ni-atoms to form hexagons around the Eu sites in accordance with the EuNi$_2$-layers of a EuNi$_5$ alloy (Fig. 1(f)). The structure of the resulting *h*-BN/EuNi$_5$/Ni(111) interface is presented in Fig. 1(c) (see the crystallographic structure in the SI). Here, *h*-BN monolayer keeps its original arrangement with respect to the Ni(111) substrate. Thus, after formation of EuNi$_5$ at the interface, N-atoms appear directly above intercalated Eu and Ni-atoms of the defected Ni-layer, whereas the B-atoms stay above the surface Ni-atoms and occupy the hollow sites above the unaffected substrate layers (Fig. 1(c)). Thus, from this consideration the (2 × 2) overstructure of the *h*-BN/EuNi$_5$/Ni(111) system with respect to the parent *h*-BN/Ni(111) interface is concluded.

Formation of an alloy yields somewhat increase in the interaction between BN and substrate ($E_{\text{ads}} = -248$ meV per BN unit cell). At that, the distance between N and underlying Eu is decreasing up to 2.95 Å, and the *h*-BN monolayer becomes slightly corrugated, leading to the mean distance between BN and the substrate equal to 3.02 Å (Fig. 3(c)).

Fig. 3(c) presents a charge redistribution at the interface between BN and EuNi$_5$/Ni(111): one can notice the local charge transfer from BN to the substrate, and also in the opposite direction. Overall, this interplay results in *n*-doped BN, although finally smaller than in the case of the sharp BN/Eu/Ni interface: the π bands are pushed by 1.16 eV to smaller binding energies as compared to BN/Eu/Ni(111) (*cf.* Fig. 2(f) and (e)). Similar to the case of the sharp interface, the presence of Eu yields a significant drop of magnetic moment at the Ni atoms located within the EuNi$_2$-sublayer of an alloy to $0.26\mu_B$. The charge redistribution due to the interface formation leads also to the shift of the 4f level by ≈30 meV to the smaller binding energies as compared to the uncovered EuNi$_5$/Ni(111) system.

Due to the lack of hybridisation between the BN π states and the valence band states of the substrate, the BN-π bands have the same shape as for the free-standing *h*-BN monolayer (*cf.* Fig. 1(f) and (a)), and magnetic moments of B/N-atoms are negligible ($m_B = 0.001\mu_B$ and $m_N = -0.001\mu_B$).

In order to further facilitate the comparison of our results with the experiment, the B 1s and N 1s core-level shifts (CLS) in X-ray photoelectron spectroscopy (XPS) and B K and N K near-edge X-ray absorption fine structure spectra (NEXAFS) were calculated for the considered interfaces.

Overall, the B/N 1s spectral lines shape is known to be affected by the interaction between the *h*-BN monolayer and a substrate.[3,10,12,45] The B 1s photoelectron spectra of the studied systems contain only one component (Fig. 4(a)). Even in the case of BN/EuNi$_5$/Ni(111), the CLS calculated for the 2 nonequivalent B atoms in the unit cell (Fig. 4(e)) only slightly differ from each other, falling within the range of 35 meV. For N 1s photoelectron spectra, the existence of two adsorption sites for N atoms with significantly different surroundings for the intercalation systems leads to the broadening of the peaks in a row BN/Ni(111) – BN/Eu/Ni(111) – BN/EuNi$_5$/Ni(111). The calculated positions of the resulting B/N 1s peaks obtained for BN/Ni(111) before and after Eu intercalation correlate with the charge redistribution at the respective interface and the corresponding doping of the *h*-BN layer. Thus, the B/N 1s spectra are shifted to large binding energies by 1.81/1.63 eV for *h*-BN/Eu/Ni(111) and by 0.61/0.37 eV for *h*-BN/EuNi$_5$/Ni(111) with respect to those positions characteristic for the parent *h*-BN/Ni(111) system (Fig. 4(a and b)).

The method of NEXAFS spectroscopy is used to study the electronic structure of the unoccupied valence band states above E_F and it is a complementary method to X-ray photoelectron spectroscopy and angle-resolved photoelectron spectroscopy used for the investigation of the energy distribution of the occupied states.

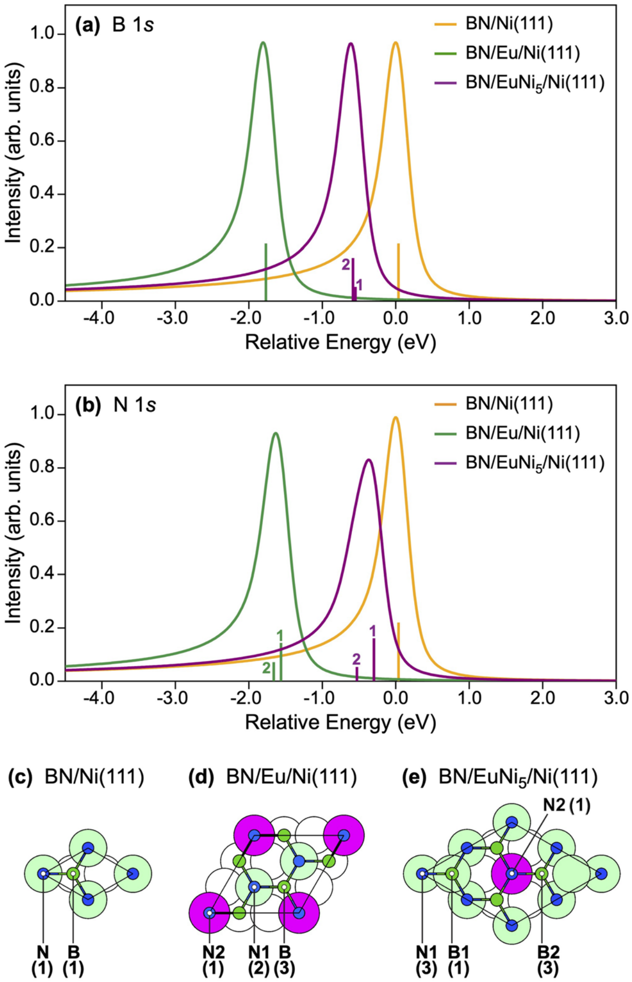

Fig. 4 (a) B 1s core level shifts obtained for the *h*-BN monolayer interfaced with Ni(111), Eu/Ni(111), and EuNi$_5$/Ni(111). (b) N 1s core level shifts obtained for the *h*-BN monolayer interfaced with Ni(111), Eu/Ni(111), and EuNi$_5$/Ni(111). (c–e) The crystallographic structures used in the calculations. Inequivalent B/N atoms in the BN layer are indicated. The corresponding weight factors are given in parentheses.

The NEXAFS spectra for the N K and B K absorption edges of *h*-BN can be separated on two energy regions: (i) 1s → π* contribution originating from the transitions of 1s core electrons of corresponding atoms into the anti-bonding π* band of *h*-BN; and (ii) 1s → σ* broad peak originating from transition of 1s core electron into the σ* bands of *h*-BN.

Fig. 5(a and b) shows the NEXAFS spectra of free-standing *h*-BN calculated for nine different incidence angles α between direction of incoming light and sample surface (*i.e.* between direction of the light's polarisation and normal to the sample's surface). One can note a smooth decreasing (increasing) weights of 1s → π* (1s → σ*) transitions when going from $\alpha = 10°$ to $\alpha = 90°$ that is in accordance with geometry of the absorption process for free-standing *h*-BN. At that, the shape and positions of the peaks[10,12,46] are well reproduced by theory.

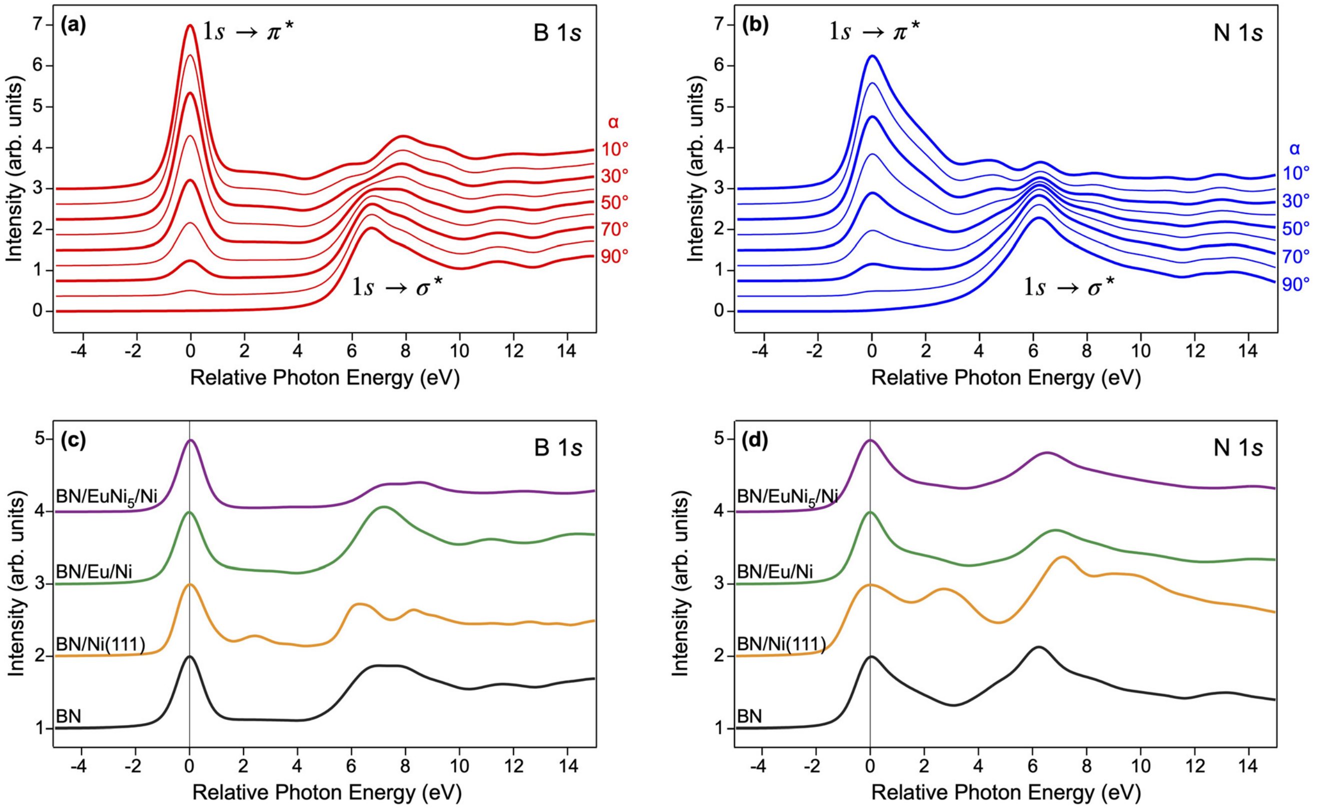

Fig. 5 (a and b) Calculated B/N K NEXAFS spectra for a free-standing *h*-BN monolayer as a function of the angle, α, between electric field vector of X-ray and the normal to the surface. (c and d) Calculated B/N K NEXAFS spectra for α = 50° for BN, BN/Ni(111), BN/Eu/Ni(111), and BN/EuNi$_5$/Ni(111).

Fig. 5(c and d) show series of the calculated B K-edge and N K-edge NEXAFS spectra for free-standing *h*-BN monolayer, BN/Ni(111), BN/Eu/Ni(111), and BN/EuNi$_5$/Ni(111). All NEXAFS spectra are presented in the relative photon energy scale with the position of the main peak for the N(B) 1s → π* transition set to 0 eV.

The *h*-BN/Ni(111) interface belongs to the class of strongly interacting interfaces. Consequently, after BN adsorption on Ni(111) the N(B) K NEXAFS spectrum is strongly modified with respect to that of free-standing *h*-BN monolayer. Firstly, in the region of the 1s → π* transition the spectra have multiple-peak structures compared to those of free-standing BN that is explained by the transitions of the respective 1s core electrons into several unoccupied states (interface states), which are the result of hybridisation of the N(B) π and Ni 3d valence band states. Secondly, one observes the visible reduction in the energy separation between the π* and σ* features as compared to that in the spectrum of free-standing BN that is a result of strong interaction between BN and a substrate, involving hybridisation between their valence band states.

When interacting with Eu/Ni and EuNi$_5$/Ni, a *h*-BN monolayer maintains its quasi free-standing nature. As a result, the B and N-absorption spectra look very similar to those of a free-standing *h*-BN monolayer. The presented theoretical XPS and NEXAFS results for different BN/Eu/Ni interfaces allow a direct comparison with the available experimental data providing clear fingerprints for the formed systems.

Following the theoretical consideration of different Eu-intercalation systems, we performed detailed structural and spectroscopic experimental studies using LEED, XPS and angle-resolved photoelectron spectroscopy (ARPES), which results are summarised in Fig. 6 and 7.

According to very good lattice match of a *h*-BN layer and Ni(111) substrate the hexagonal (1 × 1) LEED spots are observed for the parent *h*-BN/Ni(111) system (Fig. 6(a)). The deposition of thin Eu layer on top of *h*-BN/Ni(111) (see Fig. S1 in the SI) followed by the thermal annealing at 300° C for 25 min leads to the formation of the $\left(\sqrt{3} \times \sqrt{3}\right)R30°$ LEED spots as demonstrated in Fig. 6(b). This can be taken as an indication of the formation of the sharp *h*-BN/Eu/Ni(111) interface, which structure is presented in Fig. 1(b) as discussed above. Along with that, the B/N 1s XPS spectra were collected before and after intercalation of Eu in BN/Ni(111) and they reveal the energy shift of 1.83/1.2 eV to larger binding energies, respectively, relative to their positions measured for *h*-BN/Ni(111) (Fig. 6(c and d)). Taking into account the calculated XPS spectra and corresponding energy shifts (see Fig. 4), the formation of the sharp *h*-BN/Eu/Ni(111) interface is also supported by the presented XPS data (energy shifts: 1.81/1.63 eV (theory) *vs.* 1.83/1.2 eV (experiment)), since the respective calculated energy shifts of the B/N 1s XPS lines for the *h*-BN/EuNi$_5$/Ni(111) interface are much smaller.

The comparison of the experimental ARPES intensity maps, $I(k_{\|}, E_B)$, for *h*-BN/Ni(111) and *h*-BN/Eu/Ni(111) collected along

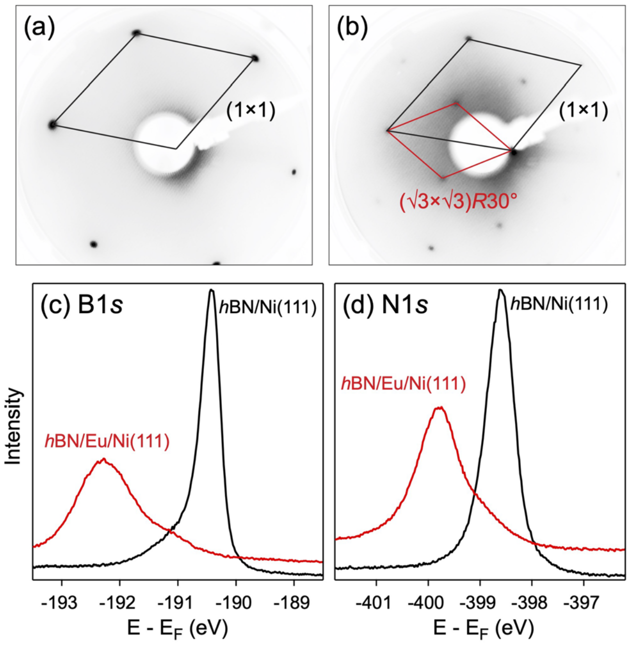

Fig. 6 LEED spots collected at a kinetic energy of 70 eV for (a) before and (b) after intercalation of Eu in *h*-BN/Ni(111). (c and d) Evolution of B 1s ($h\nu$ = 273 eV) and N 1s ($h\nu$ = 480 eV) XPS spectra during intercalation of Eu in *h*-BN/Ni(111).

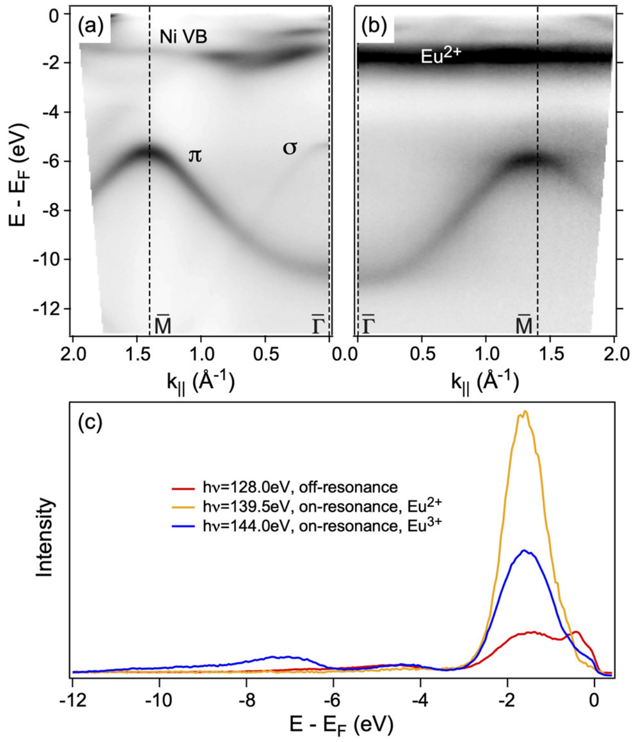

Fig. 7 ARPES intensity maps collected with photon energy of $h\nu$ = 72 eV along the $\bar{\Gamma}/\bar{M}$ direction of the *h*-BN-derived hexagonal Brillouin zone acquired (a) before and (b) after intercalation of Eu in *h*-BN/Ni(111). (c) Off- and on-resonance photoemission spectra collected after intercalation of Eu in *h*-BN/Ni(111) and taken at the Brillouin zone center.

the $\bar{\Gamma}$–$\bar{M}$ direction of the *h*-BN-derived hexagonal Brillouin zone is presented in Fig. 7(a and b), respectively. The *h*-BN-derived π and σ bands as well as Ni 3d states can be clearly identified in both ARPES maps having the respective $E(k_{\|})$ dispersions over the Brillouin zone. In case of *h*-BN/Ni(111) (Fig. 7(a)) the energy position for the π band is $E - E_F$ = −10.46/−5.63 eV at the $\bar{\Gamma}/\bar{M}$ points, respectively, which are in rather good agreement with theoretical values of $E - E_F$ = −9.69/−5.28 eV obtained for this interface within the PBE+D2 approach, as discussed above.

The intercalation of Eu atoms in the *h*-BN/Ni(111) interface does not lead to very significant changes of the $E(k_{\|})$ dispersion for both π and σ bands, as revealed by the ARPES intensity map presented in Fig. 7(b). The extracted energy position for the π band is $E - E_F$ = −10.73/−5.93 eV, at the $\bar{\Gamma}/\bar{M}$ points, respectively, thus indicating the rigid shift of ≈300 meV for this band to larger binding energies as a result of decoupling of *h*-BN-derived electronic states from those of substrate, leading to the absence of the *k*-dependent hybridisation of the respective electronic states and simple electrostatic doping of the *h*-BN layer. These experimental values for the energy position of the π band for the Eu-intercalation system can be compared with the respective values extracted from the calculated $E(k)$ dispersions for *h*-BN/Ni(111) and *h*-BN/EuNi$_5$/Ni(111) (Fig. 2(e and f)). Thus, from this analysis – shift of the π band to larger binding energies after Eu-intercalation by ≈300 meV – we can conclude on the formation of the sharp *h*-BN/Eu/Ni(111) interface. In case of the *h*-BN/EuNi$_5$/Ni(111) system, the π band is shifted to the smaller binding energies compared to its position for *h*-BN/Ni(111).

Along with that, the position of the Eu 4f band is found in ARPES data at $E - E_F$ = −1.81 eV, which is in a rather good agreement with the theoretical value of $E - E_F$ = −2.16 eV for *h*-BN/Eu/Ni(111) (*cf.* Fig. 7(b) and 2(e)) (taking into account the difficulties in the correct theoretical description of f electrons). Moreover, for the *h*-BN/EuNi$_5$/Ni(111) system these states are located at much lower binding energies of −1.33 eV (Fig. 2(f)), also supporting our previous conclusions. The Eu^{2+} valency of Eu atoms in the *h*-BN/Eu/Ni(111) system is also supported by the resonant PES spectra collected at the 4d → 4f absorption edge as demonstrated in Fig. 7(c). Considering off- and on-resonance spectra collected at $h\nu$ = 128.0 eV and $h\nu$ = 139.5 eV the strong enhancement of the divalent signal is observed, which is consistent with the previous studies for the Eu-based intermetallic compounds.[43,47] The intensity of the trivalent Eu^{3+} signal detected at $E - E_F \approx -7$ eV using photon energy of $h\nu$ = 144 eV (ref. 47) is not very significant and can be assigned to the small portion of Eu atoms diffusing in the Ni substrate during thermal annealing and formation of the sharp *h*-BN/Eu/Ni(111) interface system.

4 Conclusions

The electronic properties of systems obtained *via* intercalation of Eu in *h*-BN/Ni(111) were studied using *via* combination of state-of-the-art DFT calculations and photoelectron spectroscopy. In DFT calculations, two models were considered – sharp *h*-BN/Eu/Ni(111) interface and formation of an $EuNi_5$ alloy at the interface between BN and Ni(111). In both cases, it is found that Eu-intercalation leads to the restoring of the BN π bands together with doping of a BN layer. This effect can be attributed to the joint effect of Eu and Ni atoms at the BN–metal interface. Considering the *h*-BN/Ni(111) interface as a reference, the direction of the subsequent shift of the BN-derived π-band caused by the Eu intercalation depends on the structure of the interface layer. While in the case of the sharp interface a small downward shift of these states occurs, the formation of an interface $EuNi_5$ alloy leads to their strong shift to lower binding energies. Thus, the energy shift of the π-band obtained from BN at the Γ point and calculated core level shifts for the B/N 1s XPS lines can be considered as a fingerprint for the structure of the interface layer. Further LEED, XPS and ARPES experiments obtained on *h*-BN/Ni(111) and system formed after intercalation of Eu atom in this interface indicate the formation of the sharp *h*-BN/Eu/Ni(111) stack, which structural and electronic properties are well described by the presented DFT calculations. Our theoretical and experimental results offer the understanding on the role of rare-earth intercalation in tuning the properties of different 2D/metal interfaces and draw the way for future electronic and spintronic applications.

Conflicts of interest

There are no conflicts to declare.

Data availability

All data supporting this article have been presented within the main text and supplementary information.

Supplementary information (SI): structural data for *h*BN/Ni(111), *h*BN/Eu/Ni(111), and *h*BN/$EuNi_5$/Ni(111); LEED spots of Eu/*h*-BN/Ni(111). See DOI: https://doi.org/10.1039/d5nr03875h.

Acknowledgements

E. V. acknowledges the support by the European Union's NextGenerationEU program. Y. D. acknowledge the support by the project Centre for Advanced Laser Techniques (CALT), co-funded by the European Union through the European Regional Development Fund under the Competitiveness and Cohesion Operational Programme (Grant No. KK.01.1.1.05.0001). The authors gratefully acknowledges the computing time granted by the Resource Allocation Board and provided on the supercomputer Lise at NHR@ZIB as part of the NHR infrastructure. The calculations for this research were conducted with computing resources under the project bec00256. Experiments at Elettra were performed with the help of the beamline scientists P. Moras, P. M. Sheverdyaeva, and A. K. Kundu. This experiment has been supported by the project CALIPSOplus under Grant Agreement 730872 from the EU Framework Programme for Research and Innovation HORIZON 2020. The authors thank financial support from Spanish MINECO (MAT-2017-88374-P), PID2023-149158OB-C44 funded by MICIU/AEI/10.13039/501100011033/ and Basque Government Projects IT-1255-19 and IT-1591-22 as well as from Gipuzkoa Next program of the Diputación Foral de Gipuzkoa DFG-2023-CIEN-000077.

References

1 M. Batzill, *Surf. Sci. Rep.*, 2012, **67**, 83–115.
2 Y. Dedkov and E. Voloshina, *J. Phys.: Condens. Matter*, 2015, **27**, 303002.
3 W. Auwarter, *Surf. Sci. Rep.*, 2018, **74**, 1–95.
4 Y. Dedkov and E. Voloshina, *Nanoscale*, 2020, **12**, 11416–11426.
5 J. Yin, X. Liu, W. Lu, J. Li, Y. Cao, Y. Li, Y. Xu, X. Li, J. Zhou, C. Jin and W. Guo, *Small*, 2015, **11**, 5375–5380.
6 C. Tarrio and S. E. Schnatterly, *Phys. Rev. B: Condens. Matter Mater. Phys.*, 1989, **40**, 7852–7859.
7 Y. Kubota, K. Watanabe, O. Tsuda and T. Taniguchi, *Science*, 2007, **317**, 932–934.
8 J. Wang, F. Ma and M. Sun, *RSC Adv.*, 2017, **7**, 16801–16822.
9 K. K. Kim, H. S. Lee and Y. H. Lee, *Chem. Soc. Rev.*, 2018, **47**, 6342–6369.
10 A. B. Preobrajenski, A. S. Vinogradov and N. Mårtensson, *Phys. Rev. B: Condens. Matter Mater. Phys.*, 2004, **70**, 165404.
11 G. B. Grad, P. Blaha, K. Schwarz, W. Auwarter and T. Greber, *Phys. Rev. B: Condens. Matter Mater. Phys.*, 2003, **68**, 085404.
12 A. A. Tonkikh, E. N. Voloshina, P. Werner, H. Blumtritt, B. Senkovskiy, G. Güntherodt, S. S. P. Parkin and Y. S. Dedkov, *Sci. Rep.*, 2016, **6**, 23547.
13 A. M. I. Bakhit, K. Ali, A. A. Makarova, I. Píš, F. Bondino, R. Sant, S. P. Dash, R. Castrillo-Bodero, Y. Hasegawa, J. E. Ortega, L. Fernandez and F. Schiller, *Nanoscale*, 2023, **15**, 11517–11528.
14 G. Kresse and J. Furthmüller, *Phys. Rev. B: Condens. Matter Mater. Phys.*, 1996, **54**, 11169–11186.
15 G. Kresse and D. Joubert, *Phys. Rev. B: Condens. Matter Mater. Phys.*, 1999, **59**, 1758–1775.
16 J. P. Perdew, K. Burke and M. Ernzerhof, *Phys. Rev. Lett.*, 1996, **77**, 3865–3868.
17 P. E. Blöchl, *Phys. Rev. B: Condens. Matter Mater. Phys.*, 1994, **50**, 17953–17979.
18 P. E. Blöchl, O. Jepsen and O. K. Andersen, *Phys. Rev. B: Condens. Matter Mater. Phys.*, 1994, **49**, 16223–16233.
19 S. Grimme, *J. Comput. Chem.*, 2006, **27**, 1787–1799.
20 V. I. Anisimov, F. Aryasetiawan and A. I. Lichtenstein, *J. Phys.: Condens. Matter*, 1997, **9**, 767.
21 S. Schumacher, T. O. Wehling, P. Lazić, S. Runte, D. F. Förster, C. Busse, M. Petrović, M. Kralj, S. Blügel, N. Atodiresei, V. Caciuc and T. Michely, *Nano Lett.*, 2013, **13**, 5013–5019.

22 E. N. Voloshina and Y. S. Dedkov, *Z. Naturforsch., A:Phys. Sci.*, 2014, **69**, 297–302.

23 J. Heyd, G. E. Scuseria and M. Ernzerhof, *J. Chem. Phys.*, 2003, **118**, 8207–8215.

24 Y. Qiana and H. Yang, *Nano Today*, 2023, **53**, 102007.

25 ELSA software, https://condmat.prof/elsa (accessed: October 2025).

26 R. E. Ovcharenko, I. I. Tupitsyn, E. P. Savinov, E. N. Voloshina, B. Paulus, Y. S. Dedkov and A. S. Shulakov, *Phys. Chem. Chem. Phys.*, 2013, **15**, 6749–6756.

27 E. Voloshina, R. Ovcharenko, A. Shulakov and Y. Dedkov, *J. Chem. Phys.*, 2013, **138**, 154706.

28 A. V. Kurdyumov, V. L. Solozhenko and W. B. Zelyavski, *J. Appl. Crystallogr.*, 1995, **28**, 540–545.

29 G. Cassabois, P. Valvin and B. Gil, *Nat. Photonics*, 2016, **10**, 262–266.

30 R. J. P. Román, F. J. R. C. Costa, A. Zobelli, C. Elias, P. Valvin, G. Cassabois, B. Gil, A. Summerfield, T. S. Cheng, C. J. Mellor, P. H. Beton, S. V. Novikov and L. F. Zagonel, *2D Mater.*, 2021, **8**, 044001.

31 M. Marsman, J. Paier, A. Stroppa and G. Kresse, *J. Phys.: Condens. Matter*, 2008, **20**, 064201.

32 P. Janthon, S. A. Luo, S. M. Kozlov, F. Viñes, J. Limtrakul, D. G. Truhlar and F. Illas, *J. Chem. Theory Comput.*, 2014, **10**, 3832–3839.

33 J. Paier, M. Marsman and G. Kresse, *J. Chem. Phys.*, 2007, **127**, 024103.

34 A. V. Krukau, O. A. Vydrov, A. F. Izmaylov and G. E. Scuseria, *J. Chem. Phys.*, 2006, **125**, 224106.

35 W. Auwarter, T. Kreutz, T. Greber and J. Osterwalder, *Surf. Sci.*, 1999, **429**, 229–236.

36 M. Weser, Y. Rehder, K. Horn, M. Sicot, M. Fonin, A. B. Preobrajenski, E. N. Voloshina, E. Goering and Y. S. Dedkov, *Appl. Phys. Lett.*, 2010, **96**, 012504.

37 Y. Matsumoto, S. Entani, A. Koide, M. Ohtomo, P. V. Avramov, H. Naramoto, K. Amemiya, T. Fujikawa and S. Sakaia, *J. Mater. Chem. C*, 2013, **1**, 5533–5537.

38 K. Baberschke, *Appl. Phys. A*, 1996, **62**, 417.

39 P. Srivastava, F. Wilhelm, A. Ney, M. Farle, H. Wende, N. Haack, G. Ceballos and K. Baberschke, *Phys. Rev. B: Condens. Matter Mater. Phys.*, 1998, **58**, 5701.

40 G. Bertoni, L. Calmels, A. Altibelli and V. Serin, *Phys. Rev. B: Condens. Matter Mater. Phys.*, 2005, **71**, 075402.

41 Y. Dedkov and M. Fonin, *New J. Phys.*, 2010, **12**, 125004.

42 A. M. I. Bakhit, K. Ali and F. Schiller, *arXiv*, 2025, preprint, arXiv:2508.10746 [cond-mat.mtrl-sci], DOI: 10.48550/arXiv.2508.10746.

43 S. Wieling, S. L. Molodtsov, C. Laubschat and G. Behr, *Phys. Rev. B: Condens. Matter Mater. Phys.*, 2002, **65**, 075415.

44 F. W. Oliver, K. W. West, R. L. Cohen and K. H. J. Buschow, *J. Phys. F*, 2001, **8**, 701.

45 A. B. Preobrajenski, A. S. Vinogradov, M. L. Ng, E. Ćavar, R. Westerström, A. Mikkelsen, E. Lundgren and N. Mårtensson, *Phys. Rev. B: Condens. Matter Mater. Phys.*, 2007, **75**, 245412.

46 J. Rusz, A. B. Preobrajenski, M. L. Ng, N. A. Vinogradov, N. Mårtensson, O. Wessely, B. Sanyal and O. Eriksson, *Phys. Rev. B: Condens. Matter Mater. Phys.*, 2010, **81**, 073402.

47 W. D. Schneider, C. Laubschat, G. Kalkowski, J. Haase and A. Puschmann, *Phys. Rev. B: Condens. Matter Mater. Phys.*, 1983, **28**, 2017–2022.